JGR Space Physics

RESEARCH ARTICLE
10.1029/2023JA031601

Spectral Contamination of the 6300 Å Emission in Single-Etalon Fabry-Perot Interferometers

R. B. Kerr[1], S. Kapali[1], B. J. Harding[2], J. Riccobono[1], M. A. Migliozzi[1], J. R. Souza[3], R. Mesquita[4], P. Dandenault[4], Q. Wu[5], A. A. Pimenta[3], L. Peres[6], and R. Silva[6]

[1]Computational Physics Inc., Lowell, MA, USA, [2]Space Sciences Laboratory, University of California Berkeley, Berkeley, CA, USA, [3]National Institute for Space Research, São José dos Campos, Brazil, [4]Johns Hopkins University Applied Physics Laboratory, Laurel, MD, USA, [5]High Altitude Observatory, National Center for Atmospheric Research, Boulder, CO, USA, [6]Federal University of Western Pará, Santarém, Brazil

Key Points:

- OH airglow is an insidious spectral contaminant for single-etalon Fabry-Perot interferometers, distorting the Doppler shape of the thermospheric O^1D emission
- The consequences of OH contamination for thermospheric wind and temperature measurements vary widely between current Fabry-Perot interferometer designs
- Fabry-Perots minimize systematic 6300 Å Doppler wind errors by using an etalon spacing of 0.8676 cm plus integral multiples of 0.0826 cm

Correspondence to:
R. B. Kerr,
rkerr@cpi.com

Citation:
Kerr, R. B., Kapali, S., Harding, B. J., Riccobono, J., Migliozzi, M. A., Souza, J. R., et al. (2023). Spectral contamination of the 6300 Å emission in single-etalon Fabry-Perot interferometers. *Journal of Geophysical Research: Space Physics*, *128*, e2023JA031601. https://doi.org/10.1029/2023JA031601

Received 16 APR 2023
Accepted 10 SEP 2023

Author Contributions:
Conceptualization: R. B. Kerr, B. J. Harding, P. Dandenault, Q. Wu, R. Silva
Data curation: J. Riccobono, J. R. Souza
Formal analysis: R. B. Kerr, S. Kapali, B. J. Harding
Funding acquisition: R. B. Kerr
Investigation: R. B. Kerr, B. J. Harding, J. Riccobono, M. A. Migliozzi, J. R. Souza, R. Mesquita, P. Dandenault, Q. Wu, A. A. Pimenta, L. Peres, R. Silva
Methodology: R. B. Kerr, S. Kapali, J. Riccobono, M. A. Migliozzi, J. R. Souza, R. Mesquita, P. Dandenault, Q. Wu, A. A. Pimenta, L. Peres, R. Silva
Project Administration: R. B. Kerr

Abstract The spectral line profile of the atomic oxygen O^1D_2—$^3P_2$ transition near 6300 Å in the airglow has been used for more than 50 years to extract neutral wind and temperature information from the F-region ionosphere. A new spectral model and recent samples of this airglow emission in the presence of the nearby lambda-doubled OH Meinel (9-3) $P_2(2.5)$ emission lines underscores earlier cautions that OH can significantly distort the OI line center position and line width observed using a single-etalon Fabry-Perot interferometer (FPI). The consequence of these profile distortions in terms of the emission profile line width and Doppler position is a strong function of the selected etalon plate spacing. Single-etalon Fabry-Perot interferometers placed in the field for thermospheric measurements have widely varying etalon spacings, so that systematic wind biases caused by the OH line positions differ between instruments, complicating comparisons between sites. Based on the best current determinations of the OH and O^1D line positions, the ideal gap for a single-etalon FPI wind measurements places the OH emissions in the wings of the O^1D spectral line profile. Optical systems that can accommodate prefilters with square passbands less than ~3 Å in the optical beam can effectively block the OH contamination. When that is not possible, a method to fit for OH contamination and remove it in the spectral background of an active Fabry-Perot system is evaluated.

Plain Language Summary The bulk motion of neutral gas in the ionosphere, neutral winds, redistributes plasma creating regional ionospheric density variations and currents, which further structure ionospheric density and transport. For this reason, measurements of the neutral winds in the thermosphere are important for physics-based modeling of the ionosphere. This work revisits spectral contamination effects in a common thermospheric wind measurement technique by a nearby emission arising from the OH molecule in the upper mesosphere. Recognition of the contamination and its mitigation are essential for comparisons between and among a globally distributed array of ground-based wind measuring sites.

1. Introduction

The effects of spectral contamination by OH emission from the mesosphere on thermospheric winds and temperatures derived from Fabry-Perot interferometer (FPI) measurements of the 6300 Å OI emission are evaluated using both modeled and observed spectra. The conclusion is that the spectral contamination is insidious in all single-etalon FPI systems deployed for the measurement, and comparisons of derived temperatures and winds between sites must be accompanied by the treatment of the contamination at each location. This result is similar to the findings of Hernandez (1974).

In the middle twentieth century the sources of the metastable O^1D atom in the subauroral thermosphere were evaluated and dissociative recombination, $O_2^+ + e^- \rightarrow O(^3P) + O(^1D)$ was found to dominate relative to production by O_2 dissociation by Schumann-Runge solar ultraviolet, or photoelectron impact on O, although source efficiencies vary with local time and ionospheric conditions (Barbier & Glaume, 1962; Bates & Massey, 1947; Chamberlain, 1958; Wickwar, 1971). The 6300 Å emission in the thermosphere from O^1D radiative relaxation has a lifetime of approximately 110 s (Froese-Fischer & Saha, 1983; Garstang, 1951), so that quenching of the metastable by collision before emission is efficient in the lower thermosphere. The $O^1D \rightarrow O(^3P)$ emission layer is thus confined to a region of O^1D production by O_2^+ with atmospheric density sufficiently low to prevent quenching. Confirmation of that O^1D emission layer forming below the F2 ionospheric density peak using simultaneous

Resources: R. B. Kerr, A. A. Pimenta, L. Peres, R. Silva
Software: R. B. Kerr, S. Kapali
Supervision: R. B. Kerr
Validation: R. B. Kerr, S. Kapali, B. J. Harding, J. Riccobono, M. A. Migliozzi, J. R. Souza, R. Mesquita, Q. Wu
Visualization: S. Kapali, B. J. Harding, J. R. Souza
Writing – original draft: R. B. Kerr
Writing – review & editing: R. B. Kerr, S. Kapali, B. J. Harding, J. Riccobono, M. A. Migliozzi, J. R. Souza, R. Mesquita, P. Dandenault, Q. Wu, A. A. Pimenta, L. Peres, R. Silva

incoherent scatter ion density measurements and photometric 6300 Å measurements is demonstrated by Carlson and Weill (1967), Wickwar (1971), and Cogger et al. (1974), confirming the analytic modeling results from Chamberlain (1958).

The altitude of the 6300 Å emission layer was quickly exploited to quantify thermospheric temperatures and winds through high spectral resolution FPI measurements of the nighttime airglow emission line profile (e.g., Biondi & Feibelman, 1968; Cogger et al., 1970; Hays et al., 1969). Even earlier efforts using the FPI to sample auroral and airglow velocity distributions dating to Babcock (1923) are described by Bower (1974) and Hernandez and Killeen (1988). Early measurements of thermospheric winds derived from the Doppler shift of the 6300 Å emission are supplied by Armstrong (1969) and Hays and Roble (1971).

Amid these early efforts to remotely sample conditions in the F-region thermosphere Hernandez (1974) describes spectral contamination of the $O^1D \rightarrow O^3P$ 6300 Å emission by Meinel OH airglow. Hernandez (1974) considers three potential contaminants from the OH 9-3 vibrational band, the $P_1(2.5)$, $P_2(2.5)$, and $P_1(3.5)$ lines, and notes without position quantification that these are likely to be further Λ-doubled. (In this paper we adopt the OH Meinel transition designation convention used by Abrams et al. (1994).) Modeling these spectral contaminants in the presence of the stronger O^1D emission and as sampled by single-etalon FPIs, Hernandez (1974) considers a varying FPI free spectral range (FSR) and three order-sorting interference filter passbands. Hernandez (1974) concludes that the contamination impact is a strong function of the configured FSR, a weaker function of the relative O^1D:OH brightness, and is "never insignificant." Assessing options to remove the contamination, Hernandez (1974) notes that interference filters narrower than 8 Å (half-amplitude width centered on the O^1D emission) effectively block the OH $P_1(2.5)$ line, and that only the $P_2(2.5)$ line passes a 2.5 Å filter width used in that study.

Burnside et al. (1977) identifies all three OH 9-3 contaminants in spectrophotometer scans of the 6300 Å region. That data, collected at Arecibo near local midnight, provides the only information available on the calibrated intensity of the OH contaminants. Burnside et al. (1977) indicate that the $P_1(2.5)$, $P_2(2.5)$, and $P_1(3.5)$ lines have respective intensities of 4.2, 2.6, and 4.9 Rayleighs (R). Burnside et al. (1977) complain that the OH contamination problem had been known for "many years," yet "Papers have been published concerning airglow observations that give no discussion of a particular instrument's ability to reject the OH contamination." Burnside et al. (1977) recommends caution with geophysical parameters inferred when the O^1D emission brightness is less than 20 R.

Magee-Sauer et al. (1989) describe twin-etalon FPI spectra of Comet Halley. The terrestrial $P_2(2.5)$ OH airglow line is clearly resolved from terrestrial O^1D in their example of these spectra, supporting the recommendation of Hernandez (1974) to use two etalon FPI configurations to isolate the OH contamination from O^1D, free of order overlap. The single Magee-Sauer et al. (1989) off-comet OH $P_2(2.5)$ brightness example is roughly 10% of the terrestrial O^1D brightness, and the position of the OH $P_2(2.5)$ emission is independently calibrated to be 6297.9 Å. It is important to note that this published position is 0.09 Å lower than was specified by Hernandez (1974) and preceded the Abrams et al. (1994) work.

Despite explicit cautions expressed by Hernandez (1974) and Burnside et al. (1977), and the implicit caution of the Magee-Sauer et al. (1989) spectra, single-etalon FPI deployments for F-region measurements have proliferated using differing instrument configurations. Many of these are designed with antiquated OH line position information and none have considered quantified Λ-doubling of the OH lines. Other FPI designs apparently disregard OH spectral contamination altogether. The Madrigal database (http://cedar.openmadrigal.org/) lists 38 FPIs providing geophysical data; the earliest data set begins in 1973 at Fritz Peak. Many other international installations are unrepresented in this database (e.g., Aruliah et al., 2004; Ford et al., 2008; Ojo et al., 2022; Okoh et al., 2022; Shiokawa et al., 2003, 2012; Yatagai & Oyama, 2016; Yu et al., 2014; Yuan et al., 2010). Intercomparisons of data from various sites are common in the literature (e.g., Billett et al., 2022; Harding et al., 2017; Jiang et al., 2021; Makela et al., 2012, 2014, 2021; Meriwether, 2006; Wu et al., 2014, 2019, Xu et al., 2019). While derived horizontal winds generally compare well qualitatively, quantitative agreement has been challenging, especially for vertical winds and temperatures. A detailed treatment of OH contamination can help resolve some of these discrepancies.

In the following sections we revisit the impact of OH contamination of the O^1D 6300 Å emission using a simple spectral model with updated values of the OH (9-3) band members near the O^1D line positions. Model results are compared with data, and examples of apparent contamination effects in FPI data are shown. We conclude, as did

Table 1
Reported Air Wavelengths of OH Emissions Near 6300.304 Å

OH (9-3) transition[a]	Abrams et al. (1994) (Å)	Osterbrock et al. (1996) (Å)	Hernandez (1974) (Å)	Burnside et al. (1977) (Å)	Magee-Sauer et al. (1989) (Å)
P_1(2.5)	6287.43441[b]	6287.434		6287.4	
P_{1e} (2.5)	6287.40696				
P_{1f} (2.5)	6287.46186				
P_2(2.5)	6297.90280[b]	6297.903	6297.992 ± 0.004	6298.0	6297.9
P_{2e} (2.5)	6297.87861				
P_{2f} (2.5)	6297.92698				
P_1(3.5)	6306.92501[b]		6306.837 ± 0.009	6306.8	
P_{1e} (3.5)	6306.86882	6306.869			
P_{1f} (3.5)	6306.98119	6306.981			

[a] Emission line naming convention follows Abrams et al. (1994). Subscripts "e" and "f" denote Λ-doubled components. Subscript absence denotes unresolved Λ-doubling. [b] This value is the average of the Λ-doubled components reported by Abrams et al. (1994) and is the unresolved line position if the Λ-doubled components have equal intensity.

Hernandez (1974), that thermospheric winds and temperatures derived from measurements of the $\mathrm{O}^1\mathrm{D}$ emission line profile should be treated with caution, especially when emission rates are not reported or OH contamination is not otherwise addressed.

2. Spectral Model of 6300 Å Airglow in a Single-Etalon Fabry-Perot Interferometer

2.1. OH (9-3) Line Positions

Osterbrock et al. (1996) catalogs the spectral positions of the OH Meinel emissions in the night sky from 5200 to 8295 Å, measured with an intrinsic spectral resolution of ~0.2 Å using the high-resolution echelle spectrograph (HIRES) on the 10 m Keck telescope. The Keck-detected OH airglow spectral line positions are mapped to the calculated line positions of Abrams et al. (1994), which have a precision of 0.01 mÅ. Using Abrams et al. (1994) for wavelength calibration, Osterbrock et al. (1996) define the $\mathrm{O}^1\mathrm{D} \rightarrow \mathrm{O}^3\mathrm{P}$ emission wavelength in air to be 6300.304 Å in the Keck HIRES spectra. This is the value adopted for our modeling, and it is 0.004 Å shorter than the wavelength used by Hernandez (1974). Table 1 lists the OH line positions reported historically in the context of $\mathrm{O}^1\mathrm{D}$ spectral contamination. We adopt the Λ-doubled positions calculated by Abrams et al. (1994) for spectral modeling in this work.

Differences between the Abrams et al. (1994) OH (9-3) line positions and values used by Hernandez (1974) or Burnside et al. (1977) (listed in Table 1) are roughly one half of a FSR for an FPI gap spacing of 1 cm. In terms of realistically evaluating systematic wind and temperature errors in a single-etalon FPI, the updated line positions are essential, and used here for the first time. It is noteworthy that the twin-etalon measurement of the blended position of the P_2(2.5) Λ-doubled pair by Magee-Sauer et al. (1989) is consistent with the Abrams et al. (1994) catalog.

The positions of OH spectral contaminants in a single-etalon FPI spectrum can be manipulated to appear in the line wings of the OI 6300.304 Å emission with ideal plate spacing, to minimize the impact on derived Doppler shifts. The OH line positions known in the 1970s were considered in FPI designs at the time, accounting perhaps for the 1.26 cm gap spacing used in the Dynamics Explorer satellite FPI (Rees et al., 1982) and the 1.05 cm gap selected at Millstone Hill. Both were intended to push OH contamination to the wings of the single-etalon FPI spectrum. It does not appear that the updated line positions from the 1990s have been considered in subsequent FPI designs for thermospheric Doppler measurements.

2.2. Interferometer Response

A typical planar FPI etalon has two glass substrates, each partially mirrored on sides facing the other substrate and separated by a uniform gap. Path length differences of monochromatic light passing the etalon are ordered

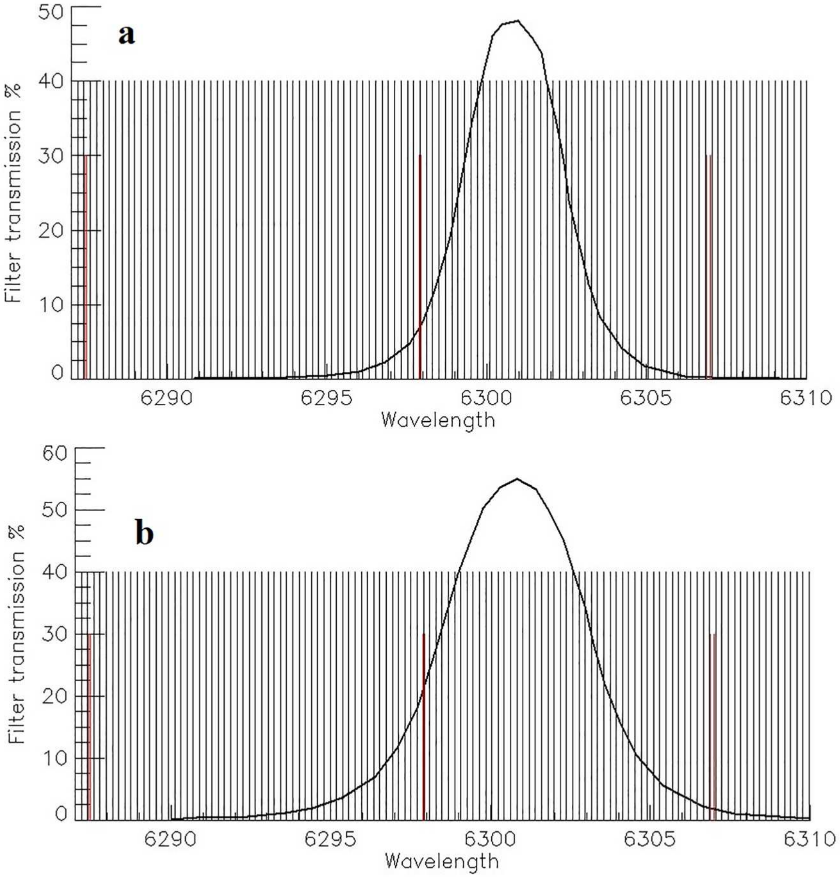

Figure 1. Spectral characteristics of two Fabry-Perot interferometer (FPI) configurations are shown. Panel (a) illustrates a 1 cm gap etalon using a 3.1 Å FWHM interference filter. Panel (b) is the same, for a 1.0192 cm gap with a 5.1 Å FWHM filter. The vertical black lines forming a comb define multiple orders of the FPI. The vertical red lines near 6287.4, 6297.9, and 6306.9 Å are the rest OH (9-3) contaminant positions. All six Λ-doubled OH lines are shown.

by multiple reflections within the gap and constructive interference of exiting rays occurs in circular annuli surrounding a central optical axis. The repeating output maxima (orders) occur at a discrete wavelength interval given by FSR = $\lambda^2/2\,\mu t$ where λ is the wavelength of the monochromatic source, μ is the index of refraction of the material in the etalon gap, and t is the gap width, or plate separation. Each successive Fabry-Perot order contains the same spectral information as the orders preceding and following.

Imaging FPIs sample multiple orders, in effect making multiple measurements in one exposure. Each order carries spatial sampling integrity through the FPI optical system, so the multiple orders can be individually analyzed to achieve multiple spectra over a region. The spatial resolution is optimized by sweeping an entire FSR over a region of camera pixels through fine gap tuning (Conde & Smith, 1995, 1998). Alternatively, multiple FPI orders imaged on a detector can be summed to enhance signal-to-noise, effectively field-widening the FPI.

Figure 1 illustrates the response of a single-etalon FPI to a 6300.304 Å (λ_0) monochromatic airglow emission. For this example, the etalon has a 1.4925 cm gap filled with dry N_2 gas. The FSR of this etalon at λ_0 is 0.1329 Å. Instrument defects broaden a monochromatic source at λ_0, and the spectral width of the λ_0 spectrum divided by the FSR defines the instrument finesse, which is a measure of the sharpness of the successive λ_0 annuli.

In practice, the light entering the FPI is not precisely monochromatic, but is distributed in a wavelength domain defined by a narrow passband prefilter. All wavelengths passing the prefilter are dispersed by the etalon, and every FPI order contains every wavelength passed. For a filter transmitting a passband (transmission function full width at half maximum, FWHM.) of 3.1 Å in a 1 cm etalon gap configuration, there are 17 full interference orders strongly passed, and several more pass through the wings of the filter transmission function beyond the FWHM position (Figure 1a).

Figures 1a and 1b show that the OH (9-3) $P_1(2.5)$ Λ-doubled lines centered at 6287.43441 Å are fully blocked by the specified prefilters. With notable exceptions (Meriwether et al., 1997; Shiokawa et al., 2012), most FPIs have used prefilter passbands sufficiently narrow to block the $P_1(2.5)$ OH emission with attenuations $>10^4$. For this reason, we do not consider the $P_1(2.5)$ OH component in our spectral model. This exclusion was also exercised by Hernandez (1974). A distribution of FPIs with 25 Å prefilters passbands centered on 6300 Å has been described by Shiokawa et al. (2012). These instruments suffer significant spectral contamination from all six nearby OH (9-3) lines, among other possible natural and manmade line sources.

We also exclude the OH (9-3) $P_1(3.5)$ Λ-doubled lines centered at 6306.92501 Å from the spectral model. Prefilter FWHM values of ∼3 Å or less and centered on λ_0 will avoid this contamination (Figure 1a). It is evident in Figure 1b that filter widths >5.0 Å begin to suffer contamination from OH (9-3) $P_1(3.5)$ lines in addition to the $P_2(2.5)$ lines. Systems with small *f*-number optics and large angles of incidence at the prefilter have larger FWHM filter characteristics than the normal-incidence transmission functions (Lissberger & Wilcock, 1959), inviting contamination by the brighter (9-3) $P_1(3.5)$ contamination.

Fisher et al. (2015), Makela et al. (2011), Makela et al. (2012), Navarro Dominguez (2020), and Shiokawa et al. (2012) describe what is now the most common FPI configuration for thermospheric wind measurements world-wide. These systems, used to validate data from space-based resources (Makela et al., 2021), feature 1.5 cm etalon gaps and *f*/4–*f*/5 (or faster) optics and interference filters with normal incidence passbands of 5–8 Å. Makela et al. (2011) and Navarro Dominguez (2020) have claimed that the 1.5 cm etalon spacing improves discrimination of OH spectral contamination. That is incorrect, and OH contamination is present in any single etalon FPI when passed by the prefilter. 1.5 cm plate spacing spreads OH (9-3) spectra throughout most of the FPI spectral FSR.

It is also claimed that the sensitivity of small aperture FPIs can be enhanced by sampling multitudes of orders using fast *f*/4-*f*/5 optics and order summing (Makela et al., 2011; Meriwether et al., 2011; Shiokawa et al., 2012). This is commonly called multiplexing. Unfortunately, fast optical systems are condemned to broadening of the prefilter transmission function, and these systems likely suffer OH spectral contamination by four Λ-doubled OH contaminants. Optical configurations that attempt to collimate the FPI optical beam for presentation to an interference filter before or after the etalon are not common in modern airglow FPI systems. Fluctuating prefilter temperatures, which move the transmission passband of classical interference filters ∼1 Å/3.7°C, also enhance the likelihood of systematically variable $P_2(2.5)$ and $P_1(3.5)$ intensities.

Despite the recent distribution of multiple FPIs likely contaminated by both the $P_1(3.5)$ and $P_2(2.5)$ lines, further modeling in this work considers only the $P_2(2.5)$ Λ-doubled lines for clarity, and because allowing $P_1(3.5)$ FPI contamination is unnecessary. The possible presence of other 9-3 components can only exacerbate contamination consequences for temperature and wind extractions relative to the outcomes described here.

Figure 2 illustrates model results for one FPI order of the example FPI with a 1.4295 cm etalon gap. With a FSR of 0.1329 Å and a finesse of 10, the intrinsic spectral resolution of the 1.4295 cm etalon gap FPI example at λ_0 is 0.01329 Å, or 632.39 m/s. (A 1.0 m/s wind produces a Doppler shift of 0.021 mÅ.) Statistical fitting to spectral profiles can produce 1-sigma uncertainties of just a few meters per second for large signal to noise data, despite the comparatively coarse instrumental resolution. However, it is instructive that small wind fitting errors from FPI configurations like this example are statistical, and do not reflect much larger systematic measurement errors that bias extractions of winds and temperatures from the fits. A fit can produce the same erroneous winds with ±1 m/s precision 66% of the time.

For accurate modeling, the wavelength of an OH contaminating emission must be known with sufficient accuracy that summing the uncertainty over multiple inter-order folds does not corrupt the relative separation of the OH line from λ_0 in an FPI order containing both. The OH (9-3) P_{2e} (2.5) line is 2.42539 ± 0.00001 Å blueward of λ_0 (Abrams et al., 1994), and folds 19 times to appear in the sampled FPI spectrum shown in Figure 2. The cumulative uncertainty in the OH line position relative to λ_0 in that spectrum is thus 0.00019 Å, equivalent to a Doppler shift of 9.04 m/s. FPI designs using smaller etalon plate spacing accumulate smaller uncertainties over fewer order-folds. The published positions of the candidate OH (9-3) contaminants are thus sufficiently accurate to model the single-etalon FPI response in terms of systematic wind and temperature errors.

The positions of the OH P_{2e} (2.5) and OH P_{2f} (2.5) in an order centered on the O^1D 6300.304 Å emission line are shown in both panels of Figure 2. Each OH feature is modeled at rest with 10% of the total intensity of the

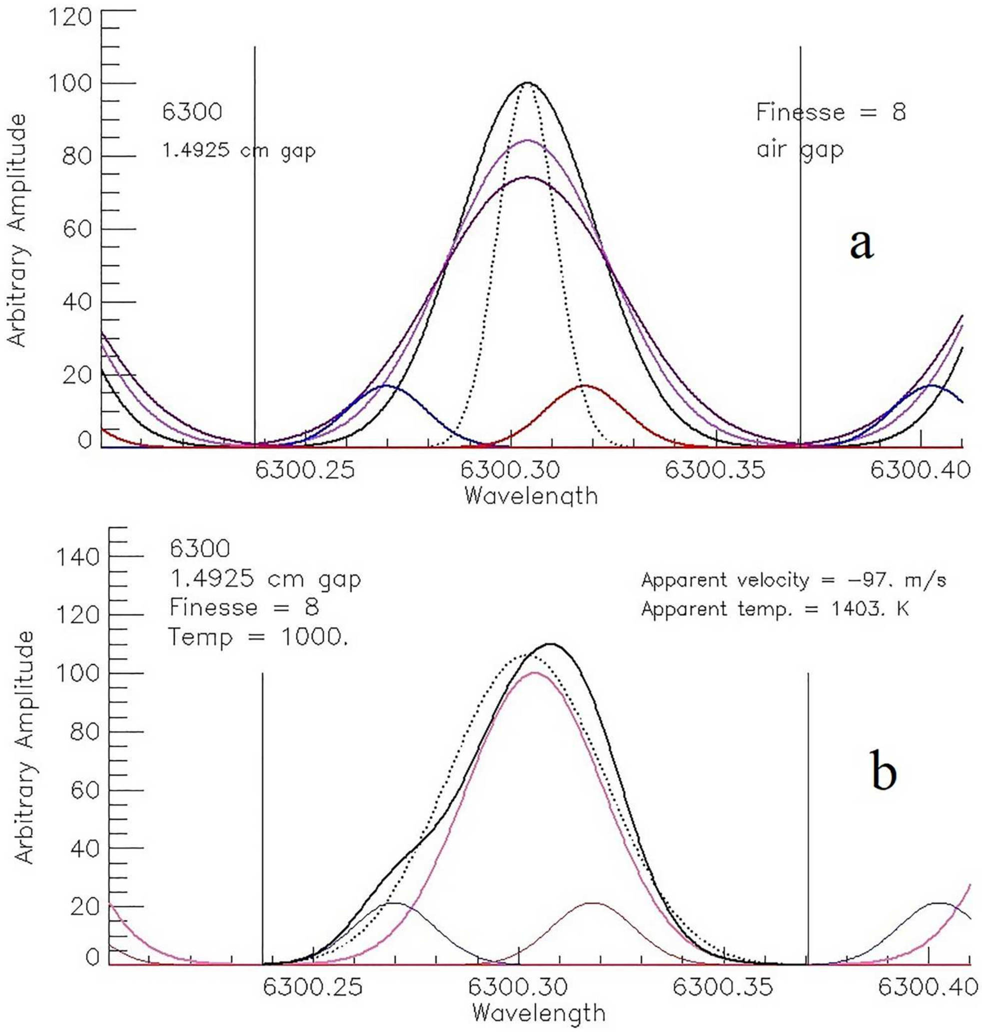

Figure 2. Panel (a) shows three OI emission profiles centered at 6300.304 Å (solid line Gaussians) with equal areas (intensities), for three temperatures, 1000, 1500, and 2000 K. The instrument function is modeled as a Gaussian with a width equal to the 1.4295 cm gap free spectral range (FSR) (0.1329 Å) divided by the finesse. This approximate instrument function is shown with the dotted line in panel (a). The FSR of this single order is shown by the vertical lines at ~6300.238 and ~6300.371 Å. Beneath the three OI line models are two OH contamination lines at 220 K, instrument broadened, each with 10% of the area (intensity) of the OI lines. The lower wavelength (blue) OH line and the upper wavelength (red) OH are each folded 19 orders from their Abrams et al. (1994) rest positions to appear in these locations. Panel (b) again shows the two OH contaminants at 10% of the OI intensity, and a 1000 K OI emission line (pink). The sum of the OH lines with the OI line is shown as the back enveloping curve, which is the model of the spectrum produced by the Fabry-Perot interferometer (FPI). A fit to that model sum is the Gaussian shown with a dotted line in panel (b), from which the apparent Doppler shift and temperature are derived. In the following sections we will show examples similar to panel (b) for some popular FPI etalon gaps.

OI line in this example. Both lines, separated by 0.04837 Å (~36% of the FSR) are folded 19 orders from their Abrams et al. (1994) line positions, and appear at 6300.25774 and 6300.30614 Å respectively, relative to the OI line, in the single-etalon spectral model. The model approximates the instrument function as a Gaussian with a width equal to FSR/finesse, and convolves the FWHM of that function with a specified O^1D temperature line width to describe the sampled spectrum. In Figure 2a 1000, 1500, and 2000 K emission temperature models are shown. The OH lines are also instrument broadened, and presumed to be characteristically thermally broadened at 220 K, a reasonable upper mesosphere value. OH lines are order-folded 19 free spectral ranges specific to their wavelengths. No continuum background sky brightness is included in the spectral model. All spectral model results described here assume that the OH line positions have no Doppler shift caused by winds that may be present near 87 km.

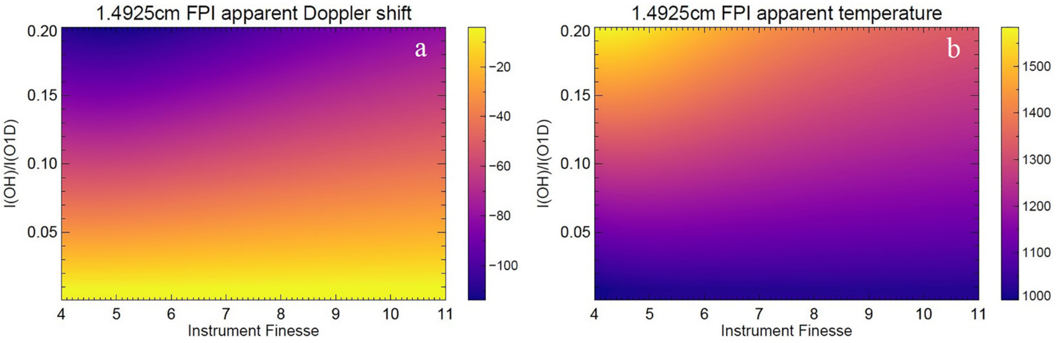

Figure 3. Panel (a) shows Doppler shifts derived from fits to modeled OI emission lines with brightness I(O1D) in the presence of OH $P_2(2.5)$ Λ-doubled emissions with total intensity I(OH), in a 1.4925 cm etalon gap design Fabry-Perot interferometer. Panel (b) shows the temperatures derived when the OH contaminants are summed with a 1000 K OI emission line. Doppler shift velocity units are m s^{-1}. Temperature units are Kelvin.

Figure 2b models a 1000 K OI emission and shows the summed spectrum of the OH and OI emissions, and a Gaussian fit to that summed spectrum with a linear background assumption. The apparent Doppler shift of the Gaussian from the 6300.304 Å rest position is −97 m/s. The temperature derived from the Gaussian FWHM is 1403 K. (The fit is a familiar Levenberg-Marquardt least squares procedure, © C.B. Markwardt 2009, within the NASA Astronomy Users Library (Astrolib) available at https://idlastro.gsfc.nasa.gov/).

The spectral positions of the $P_2(2.5)$ Λ-doubled OH contaminants in single-etalon FPI configurations depend on the configured FSR, which in turn depends on the etalon plate spacing and on the index of refraction of material within the etalon gap. Indices of refraction for CO_2, N_2, and Ar in etalon gaps used here are from Bideau-Mehu et al. (1973), Peck and Khanna (1966), and Peck and Fisher (1964), respectively. Refractive index quantification and a varying refractive index due to laboratory conditions are also potential sources of systematic error in FPI data analysis. Replacing the modeled etalon gap gas from CO_2 to Ar in Figure 2 changes the derived temperature by 0.09%, or 0.12 K. Doppler shift model values change by 0.03%, or 0.45 m/s. The gas used in the model creating Figure 2 is N_2, with a refractive index between CO_2 and Ar. Index of refraction uncertainties produce negligible systematic impacts on derived Doppler shifts and temperatures when air pressure within the etalon gap is held constant.

Figure 3 displays contour plots of the apparent Doppler shifts (Figure 3a) and temperatures (Figure 3b) for a range of FPI finesse values and ratios of OH/OI intensities. For 1.4295 cm etalon plate spacing, the OH contamination modeled in Figure 2 generates negative Doppler shifts for all contamination levels and >20 m/s blueward (negative), systematically induced Doppler shifts for any OH/OI intensity ratio exceeding 2%. Modeled temperatures are all hotter than the 1000 K model OI temperature, and exceed 1100 K with only a few percent OH/OI contamination. If we allow that the brightness of the $P_2(2.5)$ blended line is 2.6 R as measured by Burnside et al. (1977), this system produces systematically biased winds and temperatures for any OI brightness less than 130 R. This finding echoes the Hernandez (1974) assertion, that the effects of OH spectral contamination become relatively small only when the OI brightness exceeds 150 R.

Systematic Doppler shift and temperature errors are only weak functions of system finesse. We display similar results for other popular FPI etalon gaps in the following sections.

3. Data Description

The spectral model is compared with single-etalon FPI airglow spectra taken when the 6300.304 Å emission is weak and spectral contamination is evident. Data are presented from two instruments operating in Brazil, as illustrated in Figure 4. Section 4.2 describes data from an instrument located in Santarém, Brazil (hereafter the S-FPI) on 24 February 2023. The S-FPI uses 1.0192 cm etalon spacing, a prefilter with a 5.1 Å FWHM, dry CO_2 gas in the etalon gap, and a telecentric optical system. Section 4.3 compares data from the S-FPI with data from a second FPI located at Cachoeira Paulista, Brazil (hereafter the C-FPI). This comparison occurred on 27 July 2022, when both instruments were side-by-side in the optical laboratory at Cachoeira Paulista. The C-FPI uses

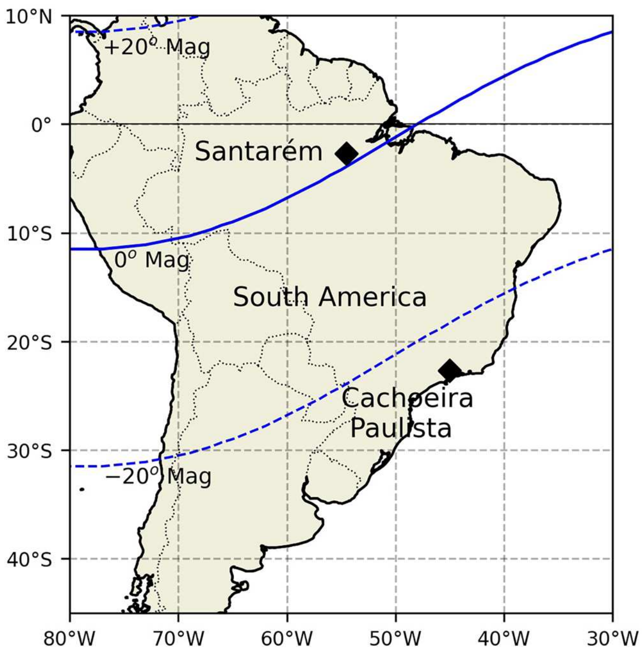

Figure 4. This work uses data from Fabry-Perot interferometers recently deployed at the two sites shown in this map. The Santarém site is very near to the intersection of the magnetic and geographic equators near the Amazon River. The Cachoeira Paulista site is a subtropical magnetic midlatitude location. In July of 2022 both instruments operated from the same laboratory at Cachoeira Paulista.

1.0204 cm etalon spacing, a 5.1 Å FWHM prefilter, dry CO_2 gas in etalon gap, and a telecentric optical system. Both the S-FPI and C-FPI are 128 mm clear aperture systems.

These instruments are owned and collaboratively operated by Instituto Nacional de Pesquisas Espaciais and the Federal University of Western Pará (UFOPA). Roughly 525 m above sea level, Cachoeira Paulista is located at 22.7°S, 45.0°W, magnetic declination and inclination 22.5°W and −40.4°, respectively. The subtropical climate features distinct seasons with cool dry winters and warm, moist summers. Average annual rainfall is ~47-inches. Santarém is located at 2.7°S, 54.5°W, magnetic declination 18.9°W and inclination −0.5°. The tropical climate is generally warm and wet, with average annual rainfall of ~55-inches. Most rain occurs distinctly in the months January through June, with drier conditions prevailing July through early December. Santerém is ~45 m above sea level.

4. Results

4.1. Spectral Models of Various FPI FSR Configurations

Figure 5 models FPIs with etalon gaps from 1.032 to 2.0 cm, in Figures 5a and 5d. Thermal and instrument broadened Λ-doubled OH (9-3) $P_2(2.5)$ lines contribute signal in broad portions of the FSR in each example, and occupy various locations in these spectra, generating a wide variety of derived Doppler shifts and temperatures from the various etalon gap configurations.

Figures 5a and 5c are examples of a class of configurations that locate the OH (9-3) $P_2(2.5)$ Λ-doubled components in the wings of the OI emission, one on each side. These configurations impose very small systematic Doppler

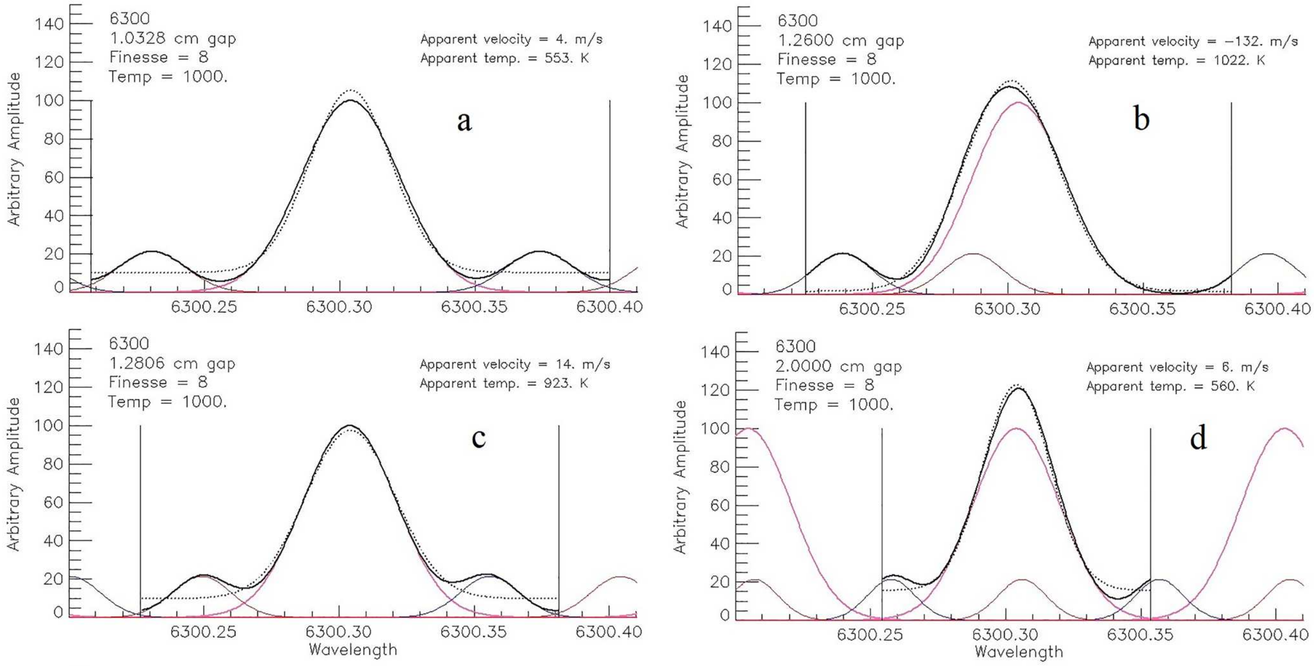

Figure 5. Four single-etalon Fabry-Perot interferometer model spectra using different etalon plate gaps are shown. Similar to Figure 2b, the free spectral range of each model is shown with vertical black lines, and the fitting analysis is performed within that wavelength domain. Each model result in these examples is for a finesse of 8, a 1000 K OI emission temperature and a 220 K OH emission temperature. Total OH intensity is modeled at 20% of the arbitrary OI brightness. The derived OI Doppler shift and temperature under these conditions are displayed at the top right of each panel.

shift errors because the OH contaminants draw the peak position of the summed spectrum equally in the blue and red spectral directions. On the other hand, the appearance of the OH lines in the OI profile wings impedes an accurate background determination. Fitting to a constant background in Figure 5a or Figure 5c (dotted line) results in background overestimation, and a corresponding increase in the spectral half-height with a decrease in the deduced FWHM. Configurations placing the OH components in the OI profile wings are susceptible to large systematic temperature errors.

One benefit of Figures 5a and 5c etalon gap family is the appearance of the OH contaminants distinct from the OI line center, so that fitting algorithms to account for the OH components are more robust. This option for mitigating the effects of OH contamination on wind and temperature extractions is further explored in Section 4.2.

Figure 5b models the spectral response of a single-etalon FPI with an etalon gap of 1.26 cm, equal to that used by the FPI onboard the Dynamics Explorer Satellite (DE) (Rees et al., 1982). This FPI illustrates another class of etalon gaps that place the arithmetic center of Λ-double OH lines in the wing of the OI emission line. The 1.26 cm gap places this location on the blue side of the OI line. That is similar and inverse to placing the OH centroid position on the red side of OI line, which is the situation for etalons with gaps near 1.05 cm, currently in use at Arecibo Optical Laboratory and the Millstone Hill Optical Laboratory.

The DE, Arecibo and Millstone FPIs were designed and placed in service shortly after the works of Hernandez (1974) and Burnside et al. (1977), and by investigators familiar with the OH contamination problem. The specific etalon gap dimensions imply that these designs may have been intended to minimize the impact of the OH (9-3) $P_2(2.5)$ contaminant, according to the published spectral positions of that blended contaminant and the OI λ_0 line position assumed at the time. Adapting the spectral model for forensic use of the Hernandez (1974) line positions places the blended OH contaminant in the wing of the OI emission line profile. Updated OH line positions from Abrams et al. (1994) and an updated λ_0 position consistent with the OH positions from Osterbrock et al. (1996) indicate that etalon gaps placing the centroid of the $P_2(2.5)$ in the OI line wing are confounded by the presence of both Λ-doubled components on each side of the centroid position.

Figure 5d illustrates a static spectral model for a 2.0 cm etalon gap, single-etalon FPI. This configuration results in OH spectral contributions across the entire, narrow FSR. By chance, the P_{2f} (2.5) line folds directly beneath line center of the OI emission line, while the P_{2e} (2.5) component appears in both wings of the FSR. Due to the spectral location of the P_{2f} (2.5) emission, this gap design generates small systematic Doppler shift errors. The OI emission line displays a true background in this configuration only for temperatures colder than commonly present in the thermosphere, while the OH contaminants further fill-in the spectral background. Due to the absence of a true spectral background sample, Gaussian fits to spectra from this configuration generate unrealistically cold temperature determinations, and the design is not generally intended for temperature determinations.

Figures 6 and 7 illustrate the entire domain of derived Doppler shifts and temperatures over a range of relative OH/OI intensities from zero to 20% and a range of finesse values between 4 and 11. Figure 6 shows these results for 1.0328 and 1.26 cm etalon gap spacing. Figure 7 shows the same for 1.2806 and 2.0 cm gap spacing.

For the family of FSR values that fold the OH (9-3) $P_2(2.5)$ components into the OI emission line background, the domain of systematic Doppler errors is small. The 1.0328 cm etalon gap (FSR = 0.1921) generates a systematic wind error between 0 and 10 m/s for all instrument finesse values >6 (Figure 6a). The derived temperatures in this configuration, assuming a constant background, are colder than the modeled 1000 K emission, due to apparent background increase with OH emission intensity (Figure 6b). Total OH emission contributions greater than 2% result in unrealistic temperature fits.

The 1.26 cm gap etalon (FSR = 0.1575 Å) generates a strongly negative (blueward) directional bias to the derived Doppler shifts (Figure 6c). Values more negative than −50 m/s are generated for OH intensity contributions greater than 4%, regardless of instrument finesse. The domain of temperature errors for this FSR (Figure 6d) are 850–1070 K, with the temperature near or slightly below the 1000 K modeled value for finesse >8 and the OH/OI intensity <10%. Greater OH intensity produces temperatures slightly above 1000 K.

Figures 7a and 7b present another example of a gap selection (1.2806 cm) placing the OH contaminants in the OI line wings (FSR = 0.1549 Å). Summed OI and OH spectra, analyzed with a Gaussian fit produce systematic Doppler shift errors over a small positive (redward) range of 0–15 m/s for all finesse values greater than seven. Temperature errors for the 1.2806 etalon spacing (Figure 7b) are weakly positive for OH/OI intensities <10%, transitioning to weakly negative excursions for larger OH contributions.

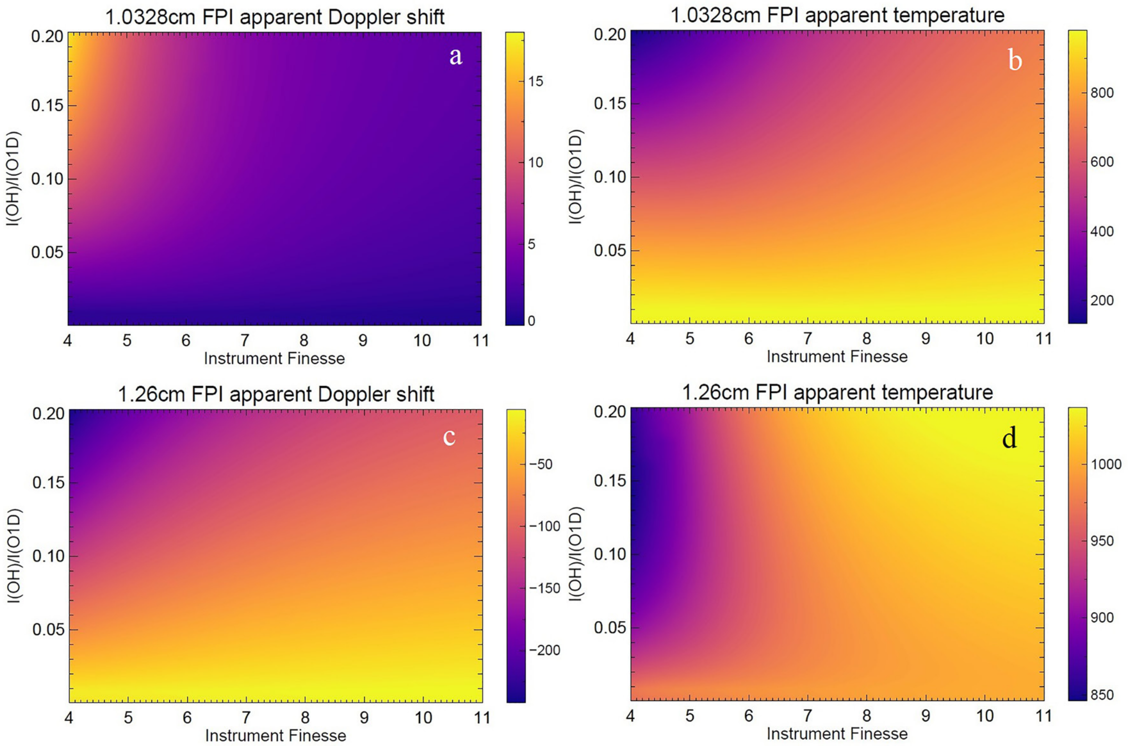

Figure 6. Similar to Figure 3, Doppler shift and temperature biases of two Fabry-Perot interferometer etalon configurations are illustrated. The derived temperatures result from spectra with a 1000 K OI emission line component added to the OH contributions. Note that each panel carries a unique derived parameter domain described by the color bars. The variations between configurations are too dramatic to meaningfully apply a uniform scale. Doppler shift velocity units are m s^{-1}. Temperature units are Kelvin.

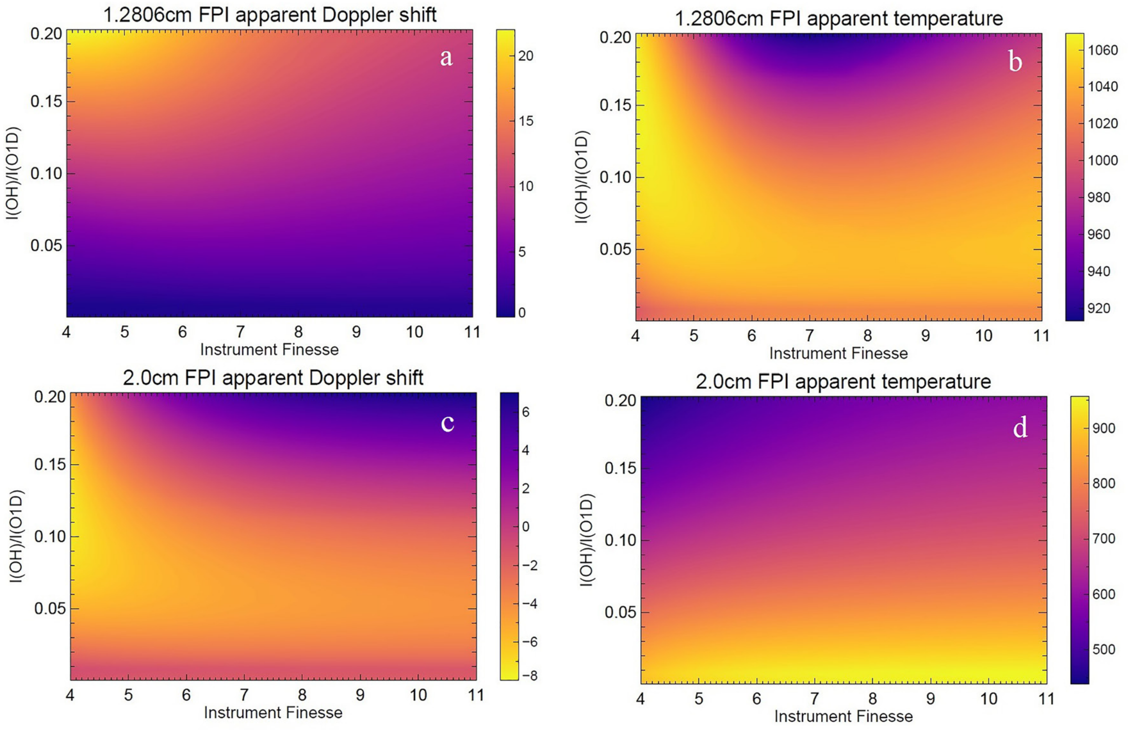

Figure 7. Similar to Figures 3 and 6, for two larger etalon gap designs. Doppler shift velocity units are m s^{-1}. Temperature units are Kelvin.

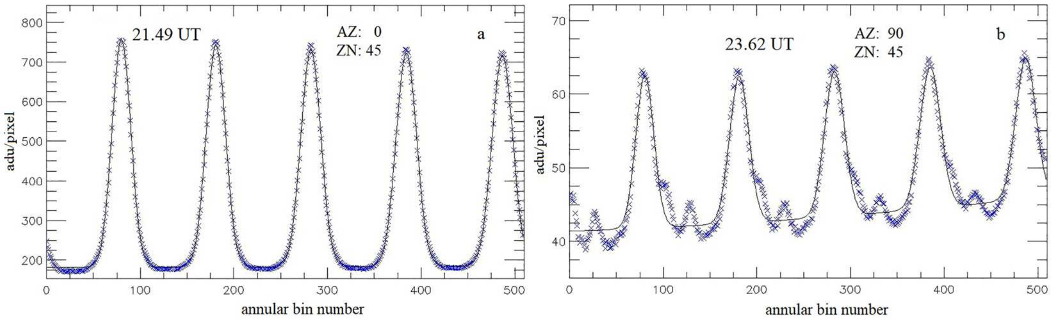

Figure 8. Raw data from an Fabry-Perot interferometer (FPI) in Santarém, Brazil, acquired on 24 February 2023 are displayed. CCD detector integration time is 180 s for both examples, and the signal is shown as analog data units (adu) per detector pixel. Signal is summed in annular bins moving outward from the FPI fringe pattern center, and the annular bin number abscissa is linear in wavelength. 4–5 orders are simultaneously imaged. The FPI pointing direction in azimuth (AZ) and zenith angle (ZN) are shown for each spectrum. Data values are indicated with blue "x" points. A five-element Gaussian fit (solid black line) applied simultaneously to the entire spectrum includes three terms for each order (line center, amplitude, and width) plus a 3-term quadratic background. Spectral contamination of the OI emission by two lines is evident on the right side of the OI emission in panel (b).

Model results for a 0.0992 Å FSR (2.0 cm etalon gap) are shown in Figures 7c and 7d. The entire domain of wind errors span −8 to +7 m/s, with small finesse dependance. Temperature measurements are not generally intended using this FSR, but Figure 6d shows that derived temperatures will always be colder than 1000 K (even for 0% OH) due to the absence of a true spectral background sample from this configuration.

4.2. Comparison With Measured FPI Spectra

The veracity of our spectral models depends upon the accuracy of the OH line positions provided by Abrams et al. (1994) and the OI λ_0 position consistent with those determinations provided by Osterbrock et al. (1996). The model indicates that certain FSR configurations leave one or both of the Λ-doubled OH (9-3) $P_2(2.5)$ spectrally distinct from the OI position, and these should be detectable in FPI spectra (e.g., Figures 5a–5c) during periods of low OI emission intensity.

Figure 8 shows two examples of 6300 Å airglow spectra from the S-FPI deployed in Santarém, Brazil. The bright OI signal in Figure 8a (signal-to-noise ∼22) overwhelms the signature of weak contaminants that may be present. In Figure 8b, the spectrum was acquired when the OI signal was low (signal-to-noise ∼3), and OH spectral contaminants become evident.

The modeled response of the S-FPI is shown in Figure 9a. The FSR of this system with 1.0192 cm etalon spacing is 194.6432 mÅ. The modeled spectrum uses the actual finesse in play during the measurements, and models for a 40% total OH intensity relative to the OI intensity. These model results are qualitatively similar to the data spectrum of Figure 8b, with a distinct feature in the background of the OI line and a second feature blended with

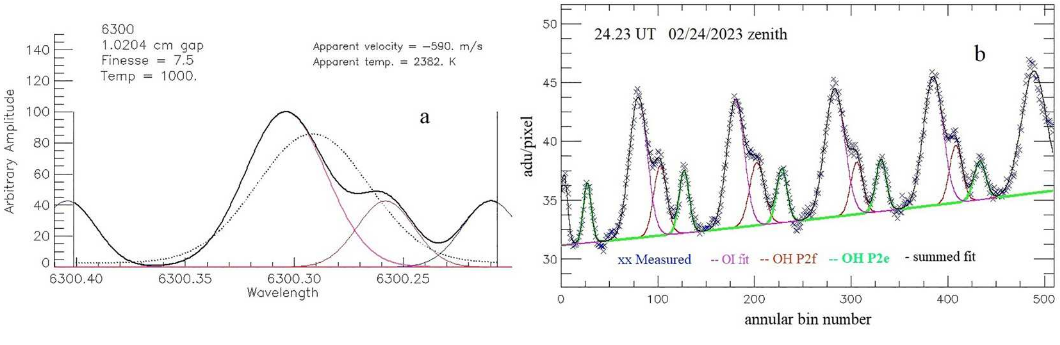

Figure 9. Panel (a) is similar to Figures 2b and 5, showing model results for a finesse of 7.5 and an OH:OI intensity ratio of 40%. Panel (b) shows a 48-term Gaussian fit to five orders of S-Fabry-Perot interferometer (FPI) data (see text). The data crosses in panel (b) were acquired with a 3-min FPI camera exposure.

the OI emission on the blue side of the OI line. Note that opposite to Figures 2 and 5, the abscissa in Figure 9a proceeds downward in wavelength. This facilitates comparison with the data spectra (Figures 8 and 9b) which also proceed red-to-blue moving out from the fringe pattern center.

Figure 9b illustrates raw data from the same instrument and night as Figure 8, during a period with weak OI emission. Geophysical data derived from the three-minute exposure in Figure 9b are not added to the processed data distributed for public use because a single Gaussian fit to one order violates several test conditions (e.g., signal-to-noise) used to classify our data in terms of reliability. Figure 9a model results demonstrate that OH contamination this strong produces unrealistic winds and temperatures when fit with a single Gaussian.

Because the spectral features in Figure 9b are so evident, we have applied a nonlinear least squares 48-term Gaussian fit across five FPI orders to the data. Each emission feature uses three Gaussian terms in each order, and a quadratic function is fit across all orders to describe the spectral background. The fit identifies two emission features in addition to the strongest OI component in each order.

The first OI fringe peaks at 81.2884 bin units in Figure 9b. The location of the feature on the high bin number shoulder of the first OI line occurs at bin number 102.6783. The distinct feature to the right of that location, in the wing of the OI line occurs at bin number 127.4049. The FSR is determined by the separation of successive OI peaks and is determined to be 100.9963 bin units. The separation between the first OI position and the spectral feature in the OI shoulder is thus 21.3899 bin units, or 0.2118 FSR, equal to 41.22 mÅ. The modeled position of the OH (9-3) P_{2f} (2.5) line after 13 order folds is 6300.26094 Å, 43.06 mÅ from the OI rest position at 6300.304 Å. The position of the shoulder feature in Figure 9b spectrum is thus 1.84 mÅ from the predicted position of the (9-3) P_{2f} (2.5) line.

The distinct feature in the wing of the OI line in Figure 9b is 46.1165 bin units from the OI position, a 88.88 mÅ separation. The model position of the OH (9-3) P_{2e} (2.5) line is 91.47 mÅ from the OI line. The distinct feature in the wing of the OI line in Figure 9b is within 2.59 mÅ of the predicted location of the OH (9-3) P_{2e} (2.5) line.

The two weaker spectral features in Figure 9b appear in FPI spectral positions consistent with the Λ-doubled OH (9-3) P_2(2.5) positions defined by Abrams et al. (1994). Conversely, the modeled Abrams et al. (1994) positions are sufficiently accurate to describe a single-etalon FPI spectrum of the 6300 Å airglow for instrument design purposes. Abrams et al. (1994) OH line positions can and should be used to model FPI configurations mitigating spectral contamination of the OI emission line.

While it appears that the positions of the P_2(2.5) Λ-doubled lines are qualitatively reproduced in FPI spectra and can be used to design FPIs with minimal OH contamination, the uncertainties remain too large to use the OH lines for the precise wavelength calibration necessary for Doppler wind extractions. Wavelength calibrations using the P_2(2.5) lines must sum uncertainties in the P_{2e} and P_{2f} fits, plus the uncertainty in the subsequent order P_{2e} line. The Abrams et al. (1994) positions provide the Å/annular bin number calibration, and successive orders of the distinct P_{2e} line calibrate the FSR. Unfortunately, our current efforts to fit the weak OH lines in five spectra produce additive line position one-sigma uncertainties that map to an OH calibrated FSR of 152.8765–227.1046 mÅ, much too coarse for Doppler wavelength calibration. For this reason, we continue to wavelength calibrate using the plate gap measured by the manufacturer using C_2H_2 C-band absorption lines.

The source of the small differences between the measured and modeled OH line positions can possibly be ascribed to winds in the upper mesosphere Doppler shifting the OH line positions, or to other small systematic uncertainties. The small differences cannot be ascribed at this time to small errors in the modeled wavelength locations specified by Abrams et al. (1994). The largest uncertainty in the FPI-sampled positions (Figure 8b) is the uncertainty in the OI λ_0 position of 6300.304 Å defined by Osterbrock et al. (1996), which carries an apparent uncertainty of ±0.001 Å. The measured OI line may also not be at rest, due to the very winds we are trying to measure. The OH line positions may also be shifted due to winds in the upper mesosphere. Similarly, the trial fit to the spectrum in Figure 8b suggests that the OH (9-3) P_{2f} (2.5) is slightly brighter than the OH (9-3) P_{2e} (2.5) emission. That is contrary to the assumption that each Λ-doubled component has equal intensity. To investigate the relative intensities one must consider the statistical fit errors, the location of each line under the rapidly sloping portion of the prefilter transmission function, and the fitting impact of a narrow CO_2 absorption feature near 15,871 cm^{-1} (Burnside et al., 1977).

4.3. Bistatic Fabry-Perot Measurements

The two FPIs briefly described in Section 3 made measurements of the airglow from Cachoeira Paulista Brazil during two nights in July 2022. Each instrument is designed to place the central position of the Λ-doubled OH

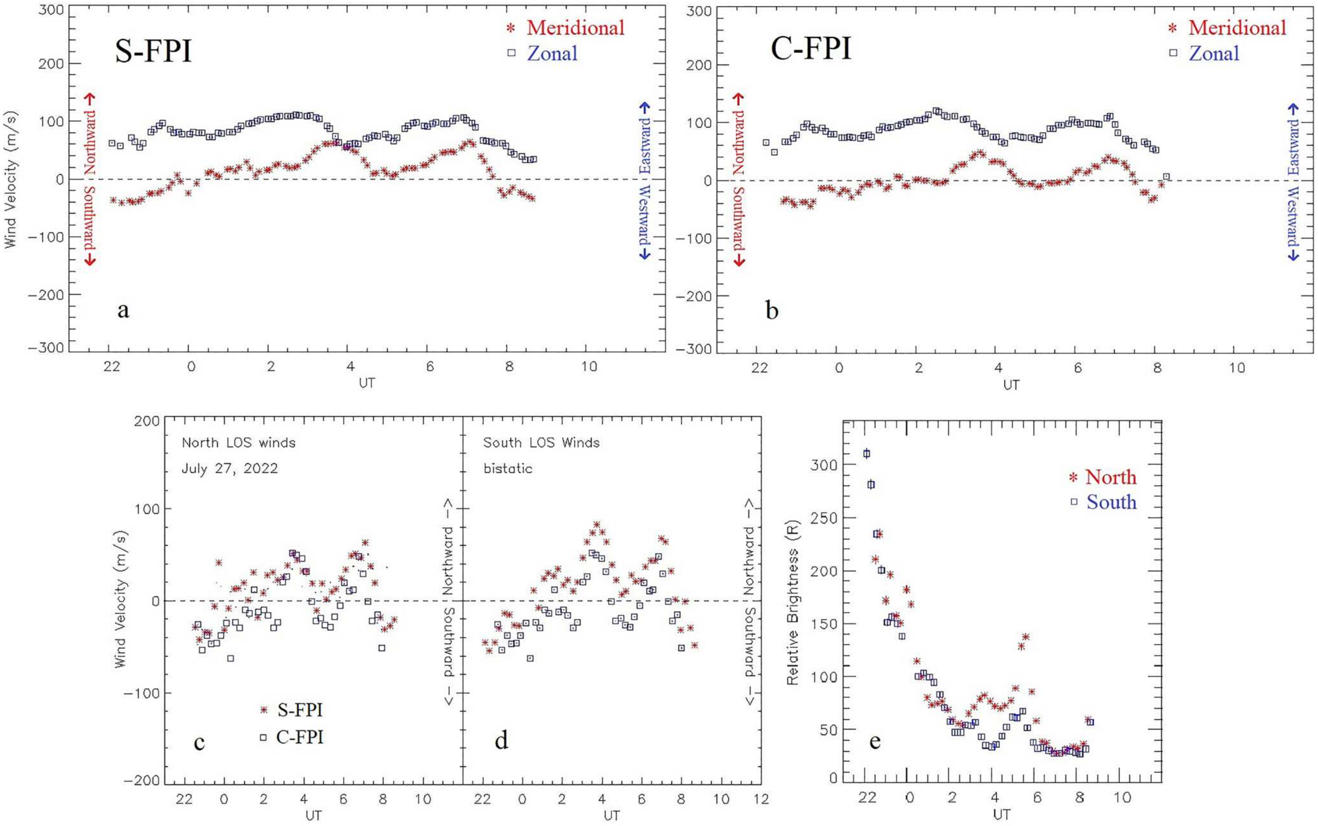

Figure 10. Panels (a, b) display the meridional (red asterisks) and zonal (blue squares) winds derived from the co-located S-Fabry-Perot interferometer (FPI) and C-FPI instruments as functions of universal time. Panel (c) shows line-of-site (LOS) winds looking North at a 45° elevation angle for both FPIs. Panel (d) is similar to panel (c), showing LOS velocities looking South at a 45° elevation angle. The OI 6300.304 Å brightness in these directions throughout the night are shown in panel (e), where red asterisks are brightness values looking North, and blue squares are the same, looking South. The brightness values for each FPI are similar, and the data in panel (e) are from the S-FPI.

(9-3) $P_2(2.5)$ line in the wing of the OI emission line, but their etalon plate spacings are slightly different. The S-FPI uses 1.0192 cm etalon spacing (0.1946 Å FSR). The C-FPI uses 1.0204 cm etalon plate spacing (0.1944 Å FSR). The prefilters in use by each instrument have similar 5.1 Å FWHM values, and Figure 1b shows the normal incidence transmission function of S-FPI prefilter.

Horizontal winds sampled by each FPI during the night of 27–28 July 2022, are shown in Figures 10a and 10b. These winds are derived from line-of-site (LOS) Doppler shifts measured in cardinal directions North, South, East and West, cosine corrected according to the 45° measurement elevation angle into the horizontal emission layer at an assumed altitude of 210 km. These horizontal North and South LOS values are then summed and averaged to approximate the effective overhead meridional wind vector. The horizontal East and West LOS values are similarly summed and averaged to quantify the overhead zonal wind vector. Vertical winds are assumed to be zero, a rest condition defined by the average of all vertical LOS Doppler shift measurements made in the zenith, during the night. This approach is the same for each FPI.

The meridional winds derived by each FPI show similar variations with time, but the magnitude of the winds derived from S-FPI data are generally larger than the meridional winds derived from C-FPI data. From ~02:00 UT onward, S-FPI meridional winds exceed the C-FPI meridional winds by roughly 25–30 m/s. Figures 10c and 10d explore the directly sampled LOS winds by each instrument in the North and South, respectively. The derived LOS winds from the S-FPI are generally larger than those from the C-FPI, and the differences are larger and more persistent in the south viewing direction after ~02:00 UT. Figure 9e shows that this period generally coincides with a weaker OI airglow emission intensity, and the intensity is particularly weak in the South viewing direction. The effects of OH spectral contamination become more pronounced as the OI intensity diminishes.

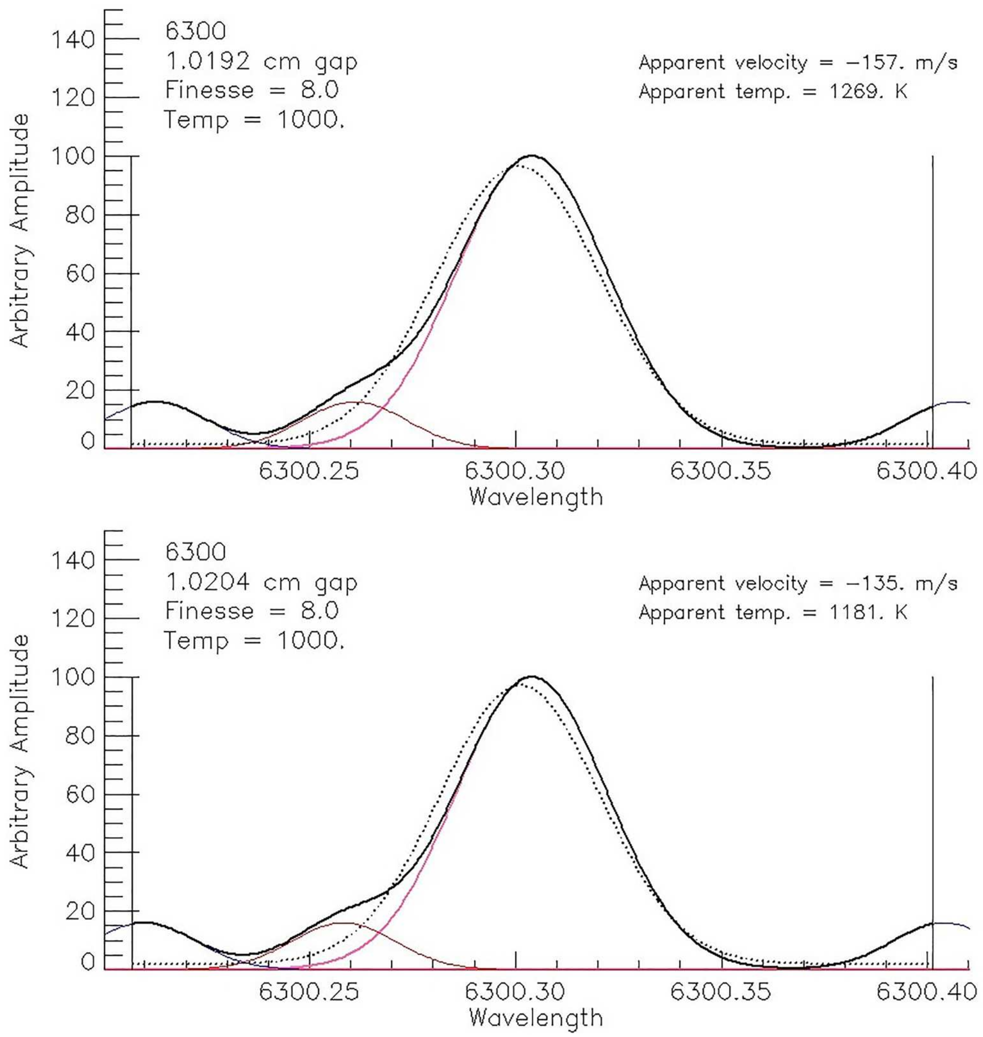

Figure 11. Similar to Figures 5 and 9a, these model results are for the S-Fabry-Perot interferometer (FPI) and C-FPI in the top and bottom panels, respectively. The modeled OH intensity totals 15% of the OI intensity. Each system imparts a negative Doppler shift bias, but the S-FPI bias is more negative by 22 m/s.

The consequences of OH spectral contamination differ between these instruments due to the slightly differing FSR values characteristic to both. Model spectra in Figure 11a shows that 15% total OH:OI brightness is expected to impart a −157 m/s systematic shift to the S-FPI spectrum. The same level of OH contamination produces a −135 m/s shift in the C-FPI spectrum. Our convention assigns a negative apparent Doppler shift to bulk motion flowing toward the observer. A negative Doppler shift looking South implies winds coming toward the observer, northward. The OH induced larger negative shifts from S-FPI are thus interpreted as stronger northward LOS winds, which qualitatively explains the apparent LOS wind discrepancy between these two instruments. That discrepancy (which also exists when looking North, but to a lesser extent due to greater OI brightness in the North after 02:00 UT) translates to a net meridional wind discrepancy when the LOS vectors are summed.

Because these instruments respond differently to the level of OH contamination, wind data discrepancies between the instruments become larger when the percentage of OH contamination becomes larger. The percentage of OH contamination increases with decreasing OI brightness, so the discrepancies become largest when the OI brightness is lowest. Unfortunately, the OH contamination induced apparent Doppler shift is not a linear function of the OH intensity fraction. Figure 12 illustrates the induced shifts in the S-FPI and C-FPI instruments. As the OH fraction increases, the differences between the derived winds in the two instruments increase. While both the S-FPI and C-FPI configurations assign a negative shift to the OI position when OH (9-3) $P_2(2.5)$ contamination is present, the S-FPI shifts are larger.

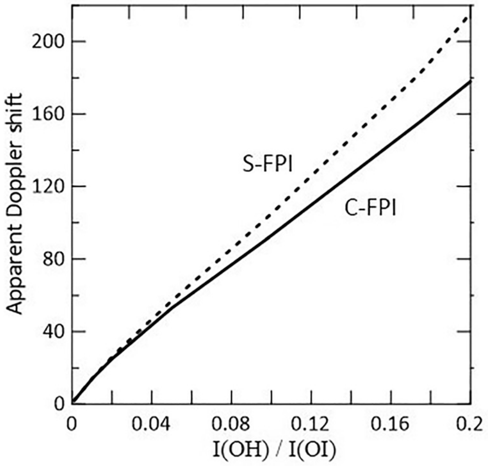

Figure 12. The apparent Doppler shift imparted by OH (9-3) $P_2(2.5)$ spectral contamination is shown as a function of the OH intensity fraction relative to the OI intensity. Both instruments produce a similar systematic ∼20 m/s Doppler shift bias when the OH intensity fraction, I(OH)/I(OI), is just 2%. As that fraction increases, the S-Fabry-Perot interferometer (FPI) bias grows larger than that produced in the C-FPI data.

Succinctly, the cause of the differing meridional wind magnitudes between these two FPIs is OH spectral contamination, and the differing instrumental responses to it. The pitfalls of data comparisons between FPIs with differing configurations are demonstrated by this bistatic measurement between very similar systems.

The effects of spectral contamination from the OH (9-3) $P_2(2.5)$ pair are present in every single-etalon FPI system now in use for the measurement of neutral winds and temperatures in the thermosphere. Moreover, the consequences for derived winds and temperatures are widely disparate between these FPIs. When the OI signal is weak, some FSR selections result in negative systematic shifts while others produce positive systematic shifts, and the magnitudes of these shifts vary dramatically.

4.4. Mitigating the Effects of OH Spectral Contamination

It may be possible to mitigate the consequences of OH contamination in single-etalon FPI spectra by fitting for the OH contaminants, commensurate with the fit to the OI emission. Using the 48-term fits described in Figure 9b, we have made an initial attempt at this strategy, applying the fits to every data exposure during the night of 24–25 February 2023 in Santarém, Brazil.

Figure 13 compares the derived thermospheric neutral winds and temperatures using our standard Gaussian least squares analysis in each order (Figures 13a and 13b) to fits assuming three Gaussians in each order (Figures 13c and 13d). Generally, the horizontal (meridional and zonal) winds are unchanged, except for the period near midnight UT. At that time the single Gaussian analysis indicates a dramatic southward excursion of the neutral meridional wind that might be attributed to an impulsive space weather event. The 3-Gaussian per order analysis (Figure 9b) reverses those data points, such that the largest sampled zonal wind of the night corresponds with the largest meridional wind of the night. Similarly, the analysis ignoring OH contamination shows a spike in neutral temperatures around UT midnight (Figure 13b). When the spectral fits include the OH (9-3) $P_2(2.5)$ Λ-doubled lines, the data indicate that neutral temperatures achieve a nighttime minimum. In general, inclusion of OH fits on this night result in lower derived temperatures than do the fits assuming no OH contaminations, by just under 100 K throughout the night.

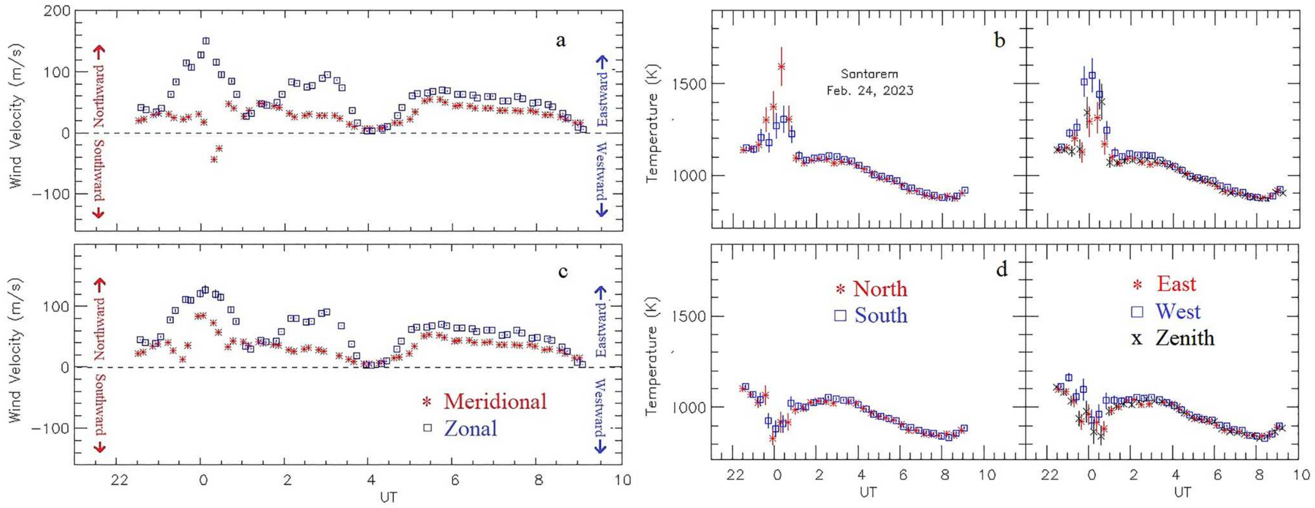

Figure 13. Panels (a, b) display F2-region winds and temperatures derived from Fabry-Perot interferometer spectral fits assuming only the OI emission is present. Panels (c, d) display these parameters when spectral fitting assumes the Λ-doubled OH (9-3) $P_2(2.5)$ emission is also present. Processed temperature data are shown for all five observation directions, north, south, east, west, and zenith.

Addressing OH spectral contamination by fitting for it would be specific to each instrument, depending on each selected FSR. Fit veracity may not be achievable for every instrument configuration, with those that render OH line positions fully beneath the OI emission profile particularly challenging. Fitting constraints setting the OH linewidths or amplitudes to be equal, or OH line positions or separations to match Abrams et al. (1994), are examples of options that might improve these fits. Wind conditions in the upper mesosphere may still confound such fitting efforts, and it is not certain that our spectral model can be sufficiently situation-specific to inform fitting models with adequate constraints to produce accurate winds and temperatures.

Another strategy to mitigate the consequences of OH spectral contamination is experimental thoroughness. A spectrometer with ∼1 Å spectral resolution can provide a critical sample of OH intensity relative to OI commensurate with FPI Doppler imaging. Knowledge of the specific FPI data susceptibility to varying levels of OH spectral contamination can then be used to assess the validity of FPI spectral fits. A general cognizance of the OH emission brightness as a function of location and season, provided by Liu et al. (2008) also provides a context for suspicious FPI wind and temperature measurements. A well characterized FPI prefilter transmission function is critical to understanding the role of OH in FPI spectra. Ideally, the filter function under circumstances approximating the FPI optical configuration (optical cone angle domain and illumination area) is the shape of merit.

The best strategy is to prevent OH contamination from being sampled in the first place. Narrow passband filters (less than ∼3 Å) with square transmission functions are expensive but can block OH contamination altogether in higher f-number optical systems. Unfortunately, this is not a viable option for most of the FPIs in service today. In those cases, the addition of a second etalon expands the FPI FSR and provides distinct spectral separation of the OH (9-3) lines from the OI line. An excellent description of multi-etalon systems and their advantages for spectral discrimination of nearby emission lines appears in Roesler, 1974.

During this analysis of $O^1D \rightarrow O^3P$ airglow, we have explored our model for the ideal single-etalon configuration to minimize the impact of OH spectral contamination. We find etalon gaps of $0.8676 + n \cdot 0.0826$ cm ($n = 0, 1, 2, 3$) produce the smallest systematic wind errors when the medium in etalon gap has a refractive index equal to one. Temperatures from these wind-idealized configurations are reliable only when the OI signal is roughly 30 times stronger than the OH signal, however.

5. Conclusions

A simple model of the airglow spectrum surrounding the OI 6300.304 Å emission as sampled by a single etalon FPI reveals insidious contamination by the OH (9-3) $P_2(2.5)$ Meinel emission. The model includes thermal and instrument broadening, inter-order overlap within the FPI spectrum, and inclusion of both P_{2e} (2.5) and P_{2f} (2.5) Λ-doubled OH components. The effects of the spectral contaminants on derived winds and temperatures depend strongly on the selected FPI FSR, and upon the relative brightness of the OH lines to the OI emission. Errors in the derived geophysical parameters are only a weak function of instrument finesse.

All single-etalon Fabry-Perot interferometers in service to sample F2-region neutral winds and temperatures suffer significant spectral contamination by the Λ-doubled OH (9-3) $P_2(2.5)$ Meinel emission. While mitigation strategies do exist, they are generally expensive, and not all are available to all instrument configurations. Isolating the OI 6300.304 Å emission for Doppler analysis in a single-etalon system is best accomplished by limiting the prefilter passband to less than 3 Å and the FPI optical *f*-number to *f*/7 or larger. Minimal systematic errors in Doppler shift derived winds are achieved when the OH contaminants are positioned in wings of the OI emission line profile, with etalon spacing of 1.0328, 1.1154, 1.1980 or 1.2806 cm. Large systematic temperature errors can only be avoided in any single-etalon FPI configuration when the OI airglow brightness is greater than ∼30 times the OH $P_2(2.5)$ total brightness.

An entire generation of ground-based and space-based FPIs intended for the measurement of F2-region winds have used FPI configurations based on faulty values for the wavelengths of the OH emissions and ignorance of the precise Λ-doubled line positions. Following the works of Abrams et al. (1994) and Osterbrock et al. (1996), a subsequent generation with a larger number of FPIs were designed and fielded without regard for OH contamination at all. The expense and toil of establishing these flawed installations is regrettable, but the scientific consequences are more troubling. While redesigning these instruments can be expensive, the present work may allow for a better quantification of uncertainty in their wind and temperature estimates.

Large excursions in FPI derived winds and temperatures have fueled several controversies. Among these are comparisons of FPI derived neutral temperatures (T_n) with differing nighttime incoherent scatter radar ion temperatures (T_i), disparate comparisons between FPI data and thermospheric temperature and wind models (e.g., Biondi & Meriwether, 1985), the search for a non-thermal OI population, and vertical winds derived from FPI measurement that appear to be unreasonably large. Sipler and Biondi (2003) and Yee (1988) describe multiple ion T_i and T_n temperature measurement discrepancies while modeling the effect of a hot neutral population on the OI emission line profile and the possible physical source of that population, respectively. Meriwether et al. (1985) draw attention to OI brightness depletions that coincide with the derivation of large equatorward winds, assessing the latter to be causal in pushing the F2 ionospheric peak density to high altitudes and reducing the OI emission rate. Makela et al. (2014) hypothesize a drizzle of particles from the plasmasphere to create large downward vertical velocities in FPI data. Large excursions in FPI data deemed non-physical have been ascribed to tropospheric scattering effects by Abreu et al. (1983) and by Harding et al. (2017). These works offering valid descriptions of systematic errors induced by highly spatially structured airglow conditions led to this reprise of the OH contamination issue, and our conclusion that OH spectral contamination is at the root of most non-physical FPI results.

Carefully configured and thoroughly characterized, ground-based FPIs provide the most accurate and economic source of thermospheric wind data available. Direct measurements of bulk motion Doppler shifts with minute-scale time resolution and nighttime local time coverage are valuable space weather information. Amortized over lifetimes commonly exceeding 50 years, instrument costs and maintenance are small. Unfortunately, the consequences of OH spectral contamination in FPI spectra vary widely between instruments, so that comparison of data from multiple sites or multiple years for geophysical insight is currently a vexed enterprise.

Establishing a common instrument configuration that mitigates the impacts of OH contamination is recommended for instruments contributing to a Space Weather data stream. In lieu of that or in the meantime, FPI data should be thoroughly scrutinized through the communication of experimental detail. To evaluate veracity, 6300 Å FPI data should always be accompanied by brightness data. Absolute brightness data are preferable but rarely available for lack of calibration equipment, while relative brightness variations are essential for evaluating possible OH contamination effects. The prefilter transmission function in an optical beam similar to the FPI optical design is an essential diagnostic to assess which of the six OH lines near 6300.304 Å may be problematic. Examples of fits to the dimmest data from which geophysical parameters are extracted can also reveal contamination issues, and questionable fits from which temperatures and winds are extracted should be identified with data quality assessments when not directly presented. Wavelength calibration detail is also essential; each experiment should stipulate if FSR values are determined by knowledge of the plate gap with uncertainties in that value, or if a wavelength calibration is otherwise applied and detailed. In addition, untangling the effects of OH contamination from a significant historical database highlights the necessity for access to raw data, which remain inaccessible for most FPIs.

Data Availability Statement

This project uses both software modeling and instrumental data. The spectral model software is written in IDL 8.8, and is available through Kerr (2023). All raw Fabry-Perot interferometer data used in this research are available without restriction through Kerr et al. (2023).

Acknowledgments
This research is supported by the National Science Foundation (NSF) Atmospheric and Geospace Sciences Division (AGS) through Grant AGS-2044771 and AGS-2030679 to Computational Physics Inc. (CPI). Research at University of California, Berkeley is supported by NSF Award AGS-1933077. Research at the Johns Hopkins Applied Physics Laboratory is supported by Grant AGS-2044782. The instruments and research described in this work are supported by the Brazilian Ministry of Science, Technology and Innovation, Brazilian Space Agency, CNPq (Grant 311840/2022-1) and the Instituto Nacional de Ciência e Tecnologia GNSS-NavAer (Grants CNPq: 465648/2014-2, FAPESP: 2017/50115-0, and CAPES: 88887.137186/2017-00).

References

Abrams, M. C., Davis, S. P., Rao, M. L. P., Engleman, R., Jr., & Brault, J. W. (1994). High-resolution Fourier transform spectroscopy of the Meinel system of OH. *Astrophysical Journal Supplement Series*, *93*, 351–395. https://doi.org/10.1086/192058

Abreu, V. J., Schmitt, G. A., Hays, P. B., Meriwether, J. W., Jr., Tepley, C. A., & Cogger, L. (1983). Atmospheric scattering effects on ground-based measurements of thermospheric winds. *Planetary and Space Science*, *31*(3), 303–310. https://doi.org/10.1016/0032-0633(83)90080-6

Armstrong, E. B. (1969). Doppler shifts in the wavelength of the OI λ6300 line in the night airglow. *Planetary and Space Science*, *17*(5), 957–974. https://doi.org/10.1016/0032-0633(69)90101-9

Aruliah, A. L., Griffin, E. M., McWhirter, I., Aylward, A. D., Ford, E. A. K., Charalambous, A., et al. (2004). First tristatic studies of meso-scale ion-neutral dynamics and energetics in the high-latitude upper atmosphere using collocated FPIs and EISCAT radar. *Geophysical Research Letters*, *31*(3), L03802. https://doi.org/10.1029/2003GL018469

Babcock, H. D. (1923). Study of the green auroral line by the interference method. *The Astrophysical Journal*, *57*, 209–221. https://doi.org/10.1086/142747

Barbier, D., & Glaume, J. (1962). La couche ionosphérique nocturne F dans la zone intertropicale et ses relations avec 1'émission de la raie 6300 Å du ciel nocturne. *Planetary and Space Science*, *9*(4), 133–149. https://doi.org/10.1016/0032-0633(62)90001-6

Bates, D. R., & Massey, H. S. W. (1947). The basic reactions in the upper atmosphere II. The theory of recombination in the ionized layers. *Proceedings of the Royal Society of London A*, 1–16.

Bideau-Mehu, A., Guern, Y., Abjean, R., & Johannin-Gilles, A. (1973). Interferometric determination of the refractive index of carbon dioxide in the ultraviolet region. *Optics Communications*, *9*(4), 432–434. https://doi.org/10.1016/0030-4018(73)90289-7

Billett, D. D., McWilliams, K. A., Kerr, R. B., Makela, J. J., Chariter, A. T., JRuohoniemi, J. M., et al. (2022). Mid-Latitude neutral wind responses to sub-auroral polarization streams. *Annales Geophysicae*, *40*(5), 571–583. https://doi.org/10.5194/angeo-40-571-2022

Biondi, M. A., & Feibelman, W. A. (1968). Twilight and nightglow spectral line shapes of oxygen 6300 and 5577 radiation. *Planetary and Space Science*, *16*(4), 431–443. https://doi.org/10.1016/0032-0633(68)90158-X

Biondi, M. A., & Meriwether, J. W., Jr. (1985). Measured response of the equatorial thermospheric temperature to geomagnetic activity and solar flux changes. *Geophysical Research Letters*, *12*(5), 267–270. https://doi.org/10.1029/GL012i005p00267

Bower, A. R. D. (1974). *A Fabry-Perot interferometer and its applications to measurement of the thermospheric temperatures and winds* (Ph.D. Thesis), F. Jacka Thesis Director. University of Adelaide.

Burnside, R. G., Meriwether, J. W., Jr., & Torr, M. R. (1977). Contamination of ground-based measurements of OI (6300Å) and NI (5200Å) airglow by OH emissions. *Planetary and Space Science*, *25*(10), 985–988. https://doi.org/10.1016/0032-0633(77)90012-5

Carlson, H. C., & Weill, G. M. (1967). Solar cycle variation of conjugate photoelectron flux onset timing deduced from 6300Å and Te observations. *Annales Geophysicae*, *23*, 569–572.

Chamberlain, J. W. (1958). Oxygen red lines in the airglow. I. Twilight and night excitation processes. *The Astrophysical Journal*, *127*, 54C–66C. https://doi.org/10.1086/146438

Cogger, L. L., Nelson, G. J., Biondi, M. R., Hake, R. D., & Sipler, D. P. (1970). Coincident F-region temperature determinations from incoherent backscatter and Doppler broadening of [OI]6300Å. *Journal of Geophysical Research*, *75*(25), 4887–4889. https://doi.org/10.1029/JA075i025p04887

Cogger, L. L., Wickwar, V. B., & Carlson, H. C. (1974). Combined airglow and incoherent scatter observations as a technique for studying neutral atmosphere variations. *Radio Science*, *9*(2), 205–210. https://doi.org/10.1029/RS009i002p00205

Conde, M., & Smith, R. W. (1995). Mapping thermospheric winds in the auroral zone. *Geophysical Research Letters*, *22*(22), 3019–3022. https://doi.org/10.1029/95GL02437

Conde, M., & Smith, R. W. (1998). Spatial structure in the thermospheric horizontal wind above Poker Flat, Alaska, during solar minimum. *Journal of Geophysical Research*, *103*(A5), 9471–9949. https://doi.org/10.1029/97JA03331.210

Fisher, D. J., Makela, J. J., Meriwether, J. W., Buriti, R. A., Benkhaldoun, Z., Kaab, M., & Lagheryeb, A. (2015). Climatologies of nighttime thermospheric winds and temperatures from Fabry-Perot interferometer measurements: From solar minimum, to solar maximum. *Journal of Geophysical Research: Space Physics*, *120*(8), 6679–6693. https://doi.org/10.1002/2015JA021170

Ford, E. A. K., Aruliah, A. L., Griffin, E. M., & McWhirter, I. (2008). Statistical analysis of thermospheric gravity waves from Fabry-Perot interferometer measurements of atomic oxygen. *Annales Geophysicae*, *26*(1), 29–45. https://doi.org/10.5194/angeo-26-29-2008

Froese-Fischer, C., & Saha, H. P. (1983). Multi-configuration Hartree-Fock results with Breit-Pauli corrections for forbidden transitions in the 2p4 configuration. *Physiological Research A*, *28*(6), 3169–3178. https://doi.org/10.1103/PhysRevA.28.3169

Garstang, R. H. (1951). Energy levels and transition probabilities in p2 and p4 configurations. *Monthly Notices of the Royal Astronomical Society*, *111*(1), 115–124. https://doi.org/10.1093/mnras/111.1.115

Harding, B. J., Makela, J. J., Qin, J., Fisher, D. J., Martinis, C. R., Noto, J., & Wrasse, C. M. (2017). Atmospheric scattering effects on ground-based measurements of thermospheric vertical wind, horizontal wind and temperature (2017). *Journal of Geophysical Research: Space Physics*, *122*(7), 7654–7669. https://doi.org/10.1002/2017JA023942

Hays, P. B., Nagy, A. F., & Roble, R. G. (1969). Interferometric measurements of the 6300Å Doppler temperature during a magnetic storm. *Journal of Geophysical Research*, *74*(16), 4162–4168. https://doi.org/10.1029/JA074i016p04162

Hays, P. B., & Roble, R. G. (1971). Direct observations of thermospheric winds during geomagnetic storms. *Journal of Geophysical Research*, *76*(22), 5316–5321. https://doi.org/10.1029/JA076i022p05316

Hernandez, G. (1974). Contamination of the OI ($^3P_2$ – $^1D_2$) emission line by the (9-3) band of OH X^{2}II in high-resolution measurements of the night sky. *Journal of Geophysical Research*, *79*(7), 1119–1123. https://doi.org/10.1029/JA079i007p01119

Hernandez, G., & Killeen, T. L. (1988). Optical measurements of winds and kinetic temperatures in the upper atmosphere. *Advances in Space Research*, *8*(5–6), (5)149–(5)213. https://doi.org/10.1016/0273-1177(88)90042-7

Jiang, G., Xiong, C., Stolle, C., Xu, J., Yuan, W., Makela, J. J., et al. (2021). Comparison of thermospheric winds measured by GOCE and ground-based FPIs at low and middle latitudes. *Journal of Geophysical Research: Space Physics*, *126*(2), 16. https://doi.org/10.1029/2020JA028182

Kerr, R. B. (2023). Spectral contamination of the 6300Å emission in single-etalon Fabry-Perot interferometers – Software. Zenodo. https://doi.org/10.5281/zenodo.8226372

Kerr, R. B., Kapali, S., Harding, B. J., & Souza, J. R. (2023). Spectral contamination of the 6300Å emission in single-etalon Fabry-Perot interferometers – Data. Zenodo. https://doi.org/10.5281/zenodo.8225839

Lissberger, P. H., & Wilcock, W. L. (1959). Properties of all-dielectric interference filters. II. Filters in parallel beams of light incident obliquely and in convergent beams. *Journal of the Optical Society of America A*, *49*(2), 126–130. https://doi.org/10.1364/JOSA.49.000126

Liu, G., Shepherd, G. G., & Roble, R. G. (2008). Seasonal variations of the nighttime O^{1}S and OH airglow emission rates at mid-to-high latitudes in the context of large-scale circulation. *Journal of Geophysical Research*, *113*(A6), A06302. https://doi.org/10.1029/2007JA012854

Magee-Sauer, L., Scherb, F., Roessler, F. L., Harlander, J., & Lutz, B. L. (1989). Fabry-Perot observations of NH$_2$ emission from Comet Halley. *Icarus*, *83*(1), 50–60. https://doi.org/10.1016/0019-1035(89)90022-5

Makela, J. J., Baughman, M., Navarro, L. A., Harding, B. J., Englert, C. R., Harlander, J. M., et al. (2021). Validation of ICON-MIGHTI thermospheric wind observations: 1. Nighttime red-line ground-based Fabry-Perot interferometers. *Journal of Geophysical Research: Space Physics*, *126*(2), 13. https://doi.org/10.1029/2020JA028726

Makela, J. J., Harding, B. J., Meriwether, J. W., Mesquita, R., Sanders, S., Ridley, A. J., et al. (2014). Storm time response of the midlatitude thermosphere: Observations from a network of Fabry-Perot interferometers. *Journal of Geophysical Research: Space Physics*, *119*(8), 6758–6773. https://doi.org/10.1002/2014JA019832

Makela, J. J., Meriwether, J. W., Huang, Y., & Sherwood, P. J. (2011). Simulation and analysis of a multi-order imaging Fabry-Perot interferometer for the study of thermospheric winds and temperatures. *Applied Optics*, *50*(22), 4403–4416. https://doi.org/10.1364/AO.50.004403

Makela, J. J., Meriwether, J. W., Ridley, A. J., Ciocca, M., & Castellez, M. W. (2012). Large-scale measurements of thermospheric dynamics with a multisite Fabry-Perot interferometer network: Overview of plans and results from midlatitude measurements. *International Journal of Geophysics*, *2012*, 10. https://doi.org/10.1155/2012/872140

Meriwether, J. W. (2006). Studies of thermospheric dynamics with a Fabry-Perot interferometer network: A review. *Journal of Atmospheric and Solar-Terrestrial Physics*, *68*(13), 1576–1589. https://doi.org/10.1016/j.jastp.2005.11.014

Meriwether, J. W., Biondi, M. A., Herrero, F. A., Fesen, C. G., & Hallenback, D. C. (1997). Optical interferometric studies of the nighttime equatorial thermosphere: Enhanced temperatures and zonal wind gradients. *Journal of Geophysical Research*, *12*(A9), 20041–20058. https://doi.org/10.1029/97JA01463

Meriwether, J. W., Makela, J. J., Huang, Y., Fisher, D. J., Buriti, R. A., Medeiros, A. F., & Takahashi, H. (2011). Climatology of the nighttime equatorial thermospheric winds and temperatures over Brazil near solar minimum. *Journal of Geophysical Research*, *116*(A4), 148–227. https://doi.org/10.1029/2011JA016477

Meriwether, J. W., Jr., Biondi, M. A., & Anderson, D. A. (1985). Equatorial airglow depletions induced by thermospheric winds. *Geophysical Research Letters*, *12*(8), 487–490. https://doi.org/10.1029/GL012i008p00487

Navarro Dominguez, L. A. (2020). *Storm-time equatorial thermospheric Dynamics and electrodynamics* (Ph.D. Thesis), B. Fejer Thesis Director. Utah State University. https://doi.org/10.26076/a730-262

OjoKatamzi-Joseph, T. Y. Z. T., Chu, K. T., Grawe, M. A., & Makela, J. J. (2022). A climatology of the nighttime thermospheric winds over Sutherland, South Africa. *Advances in Space Research*, *69*(1), 209–219. https://doi.org/10.1016/j.asr.2021.10.015

Okoh, D., Bounhir, A., Habarulema, J. B., Rabiu, B., Katamzi-Joseph, Z., Ojo, T., et al. (2022). Thermospheric neutral wind measurements and investigations across the African region - A review. *Atmosphere*, *13*(6), 863. https://doi.org/10.3390/atmos13060863

Osterbrock, D. E., Fulbright, J. P., Martel, A. R., Keane, M. J., Träger, S. C., & Basri, G. (1996). Night-sky high-resolution spectral atlas of OH and O_2 emission lines for echelle spectrograph wavelength calibration. *Publications of the Astronomical Society of the Pacific*, *108*, 2770308. https://doi.org/10.1086/133920

Peck, E. R., & Fisher, D. J. (1964). Dispersion of argon. *Journal of the Optical Society of America A*, *54*(11), 1362–1364. https://doi.org/10.1364/JOSA.54.001362

Peck, E. R., & Khanna, B. N. (1966). Dispersion of nitrogen. *Journal of the Optical Society of America A*, *56*(8), 1059–1063. https://doi.org/10.1364/JOSA.56.001059

Rees, D., Fuller-Rowell, T. J., Lyons, A., Killeen, T. L., & Hays, P. B. (1982). Stable and rugged etalon for the dynamics explorer Fabry-Perot interferometer. 1: Design and construction. *Applied Optics*, *21*(21), 3896–3902. https://doi.org/10.1364/AO.21.003896

Roesler, F. (1974). Fabry-Perot instruments for Astronomy. In N. Carleton (Ed.), *Methods in experimental physics* (pp. 531–569). Academic Press. https://doi.org/10.1016/S0076-695X(08)60504-9

Shiokawa, K., Kadota, T., Otsuka, Y., Ogawa, T., Nakamura, T., & Fukao, S. (2003). A two-channel Fabry-Perot interferometer with thermoelectric-cooled CCD detectors for neutral wind measurement in the upper atmosphere. *Earth Planets and Space*, *55*(5), 271–275. https://doi.org/10.1186/BF03351759

Shiokawa, K., Otsuka, Y., Oyama, S., Nozawa, S., Satoh, M., Katoh, Y., et al. (2012). Development of low-cost sky-scanning Fabry-Perot interferometers for airglow and auroral studies. *Earth Planets and Space*, *64*(11), 1033–1046. https://doi.org/10.5047/eps.2012.05.004

Sipler, D. P., & Biondi, M. A. (2003). Simulation of hot oxygen effects on ground-based Fabry-Perot determinations of thermospheric temperatures. *Journal of Geophysical Research*, *108*(A6), 1260–1266. https://doi.org/10.1029/2003JA009911

Wickwar, V. B. (1971). *Photoelectrons from the magnetic conjugate point studied by means of the 6300Å predawn enhancement and the plasma line enhancement* (Ph.D. Thesis), W.E. Gordon Thesis Director. Rice University.

Wu, Q., Sheng, C., Wang, W., Noto, J., Kerr, R., McCarthy, M., et al. (2019). The midlatitude thermospheric dynamics from an interhemispheric perspective. *Journal of Geophysical Research: Space Physics*, *124*(10), 7971–7983. https://doi.org/10.1029/2019JA026967

Wu, Q., Yuan, W., Xu, J., Huang, C., Zhang, S., Wang, J.-S., & Li, T. (2014). First U.S.-China joint ground-based Fabry-Perot interferometer observations of longitudinal variations in the thermo-spheric winds. *Journal of Geophysical Research: Space Physics*, *119*(7), 5755–5763. https://doi.org/10.1002/2014JA020089

Xu, H., Shiokawa, K., Oyama, S., & Nozawa, S. (2019). High-latitude thermospheric wind study using a Fabry-Perot interferometer at Tromsø in Norway: Averages and variations during quiet times. *Earth Planets and Space*, *71*(1), 1–8. https://doi.org/10.1186/s40623-019-1093-8

Yatagai, A., & Oyama, S.-I. (2016). Thermospheric nocturnal wind climatology observed by Fabry-Perot interferometers over the Asia–Oceania region. *Journal of the Meteorological Society of Japan. Ser. II*, *94*(6), 525–536. https://doi.org/10.2151/jmsj.2016-026

Yee, J.-H. (1988). Non-thermal distribution of O1D atoms in the night-time thermosphere. *Planetary and Space Science*, *36*(1), 89–97. https://doi.org/10.1016/0032-0633(88)90149-3

Yu, T., Huang, C., Zhao, G., Mao, T., Wang, Y., Zeng, Z., et al. (2014). A preliminary study of thermosphere and mesosphere wind observed by Fabry-Perot over Kelan, China. *Journal of Geophysical Research: Space Physics*, *119*(6), 4981–4997. https://doi.org/10.1002/2013JA019492

Yuan, W., Xu, J., Ma, R., Wu, Q., Jiang, F., Gao, H., et al. (2010). First observation of mesospheric and thermospheric winds by a Fabry-Perot interferometer in China. *Chinese Science Bulletin*, *55*(35), 4046–4051. https://doi.org/10.1007/s11434-010-4192-2